Title

Iron and Carbon Dynamics during Aging and Reductive Transformation of Biogenic Ferrihydrite

Journal

Environmental Science and Technology, 50(1)

ISSN

0013-936X

Authors

Cismasu, A Cristina
Williams, Kenneth H
Nico, Peter S

Publication Date

2016-01-05

DOI

10.1021/acs.est.5b03021

Peer reviewed

Iron and Carbon Dynamics during Aging and Reductive Transformation of Biogenic Ferrihydrite

A. Cristina Cismasu[*†], Kenneth H. Williams[†], and Peter S. Nico[†]

[†] Lawrence Berkeley National Laboratory, 1 Cyclotron Rd., Berkeley, California, United States

Environ. Sci. Technol., **2016**, *50* (1), pp 25–35

DOI: 10.1021/acs.est.5b03021

Publication Date (Web): November 25, 2015

*Phone: 650-644-8588; e-mail: accismasu@lbl.gov.

Abstract

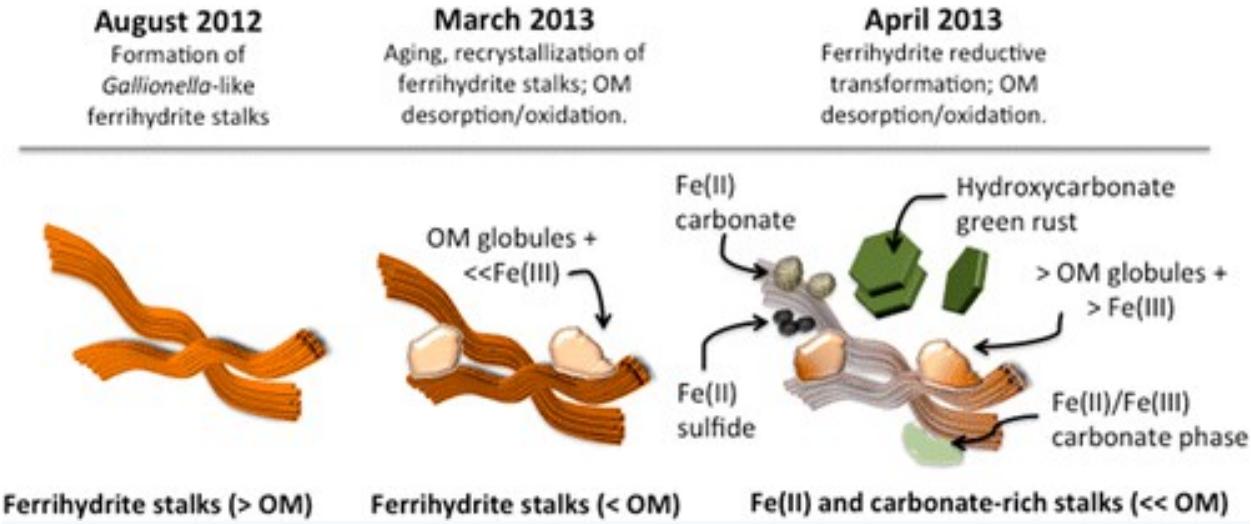

Natural organic matter is often associated with Fe(III) oxyhydroxides, and may be stabilized as a result of coprecipitation or sorption to their surfaces. However, the significance of this association in relation to Fe and C dynamics and biogeochemical cycling, and the mechanisms responsible for organic matter stabilization as a result of interaction with minerals under various environmental conditions (e.g., pH, Eh, etc.) are not entirely understood. The preservation of mineral-bound OM may be affected by OM structure and mineral identity, and bond types between OM and minerals may be central to influencing the stability, transformation and composition of both organic and mineral components under changing environmental conditions. Here we use bulk and submicron-scale spectroscopic synchrotron methods to examine the in situ transformation of OM-bearing, biogenic ferrihydrite stalks (*Gallionella ferruginea*-like), which formed following injection of oxygenated groundwater into a saturated alluvial aquifer at the Rifle, CO field site. A progression from oxidizing to reducing conditions during an eight-month period triggered the aging and reductive transformation of *Gallionella*-like ferrihydrite stalks to Fe (hydroxy)carbonates and Fe sulfides, as well as alteration of the composition and amount of OM. Spectromicroscopic measurements showed

a gradual decrease in reduced carbon forms (aromatic/alkene, aliphatic C), a relative increase in amide/carboxyl functional groups and a significant increase in carbonate in the stalk structures, and the appearance of organic globules not associated with stalk structures. Biogenic stalks lost ~30% of their initial organic carbon content. Conversely, a significant increase in bulk organic matter accompanied these transformations. The character of bulk OM changed in parallel with mineralogical transformations, showing an increase in aliphatic, aromatic and amide functional groups. These changes likely occurred as a result of an increase in microbial activity, or biomass production under anoxic conditions. By the end of this experiment, a substantial fraction of organic matter remained in identifiable Fe containing stalks, but carbon was also present in additional pools, for example, organic matter globules and iron carbonate minerals.

Introduction

The association of organic matter (OM) with ferric iron oxyhydroxides is recognized as a key process in the stabilization of OM in surface environments.(1-5) Owing to the ubiquity of iron and organic carbon in soils, surface waters, and aquifers, and to the high specific surface area and reactivity of Fe(III) oxyhydroxides, this association may have a substantial impact on OM stabilization. Occlusion of organic matter within mineral coprecipitates, as well as OM chemical structure and bond strength between OM and minerals may impact its preservation.(1, 2, 6, 7)Alternatively, Fe(III) oxyhydroxide sorbent types may also play key roles in OM preservation(1)due to their variable surface areas and reactivities. A mechanistic understanding of the processes involved in the formation and stabilization of Fe(III) oxyhydroxide-OM associations is currently lacking, particularly regarding sorbed OM structure, localization, conformation,(1) and potential stages of OM degradation as a result of environmental drivers that govern both C and Fe biogeochemical cycles (changes in pH, redox conditions, microbial community composition, etc.).

Ferrihydrite is among the most widespread Fe(III) oxyhydroxides at the earth's surface, often forming at redox boundaries as a result of rapid Fe(II) oxidation. It is known for its nanoparticulate nature, poor crystallinity, high surface area and reactivity. It is commonly associated with organic carbon in soils, sediments,(8) as well as freshwater, marine,(5, 9) and hydrothermal settings,(10, 11) with frequent organic-matter–ferrihydrite associations occurring as a result of biomineralization by Fe(II) oxidizing microorganisms.(11-16) The exposure of ferrihydrite to fluctuating redox conditions triggers recrystallization or mineralogical transformations that impact the chemical speciation, mobility, and

bioavailability of associated major or trace elements.(17) Ferrihydrite aging and (a)biotic transformation rates, as well as the types of secondary minerals depend on phase purity, for example, sorption/incorporation of Al, Si, P, or organic matter.(11, 18-23) It is anticipated that mineral transformations will also affect the speciation of ferrihydrite-bound natural organic matter; OM can exchange or shuttle electrons(23, 24) but it may also oxidize or desorb selectively.

The objective of this work is to present an example of Fe and C dynamics during the aging and reductive transformation of a biogenic ferrihydrite precipitated in situ within the saturated aquifer at the U.S. Department of Energy (DOE) Rifle, CO test site.(23) OM-bearing precipitates dominated by *Gallionella*-like ferrihydrite stalks formed during a forced oxidation event (injection of oxygenated water into the subsurface); the aging and reductive transformation of the precipitate was monitored for a period of eight months (between August 2012 and April 2013) as groundwater reverted to reducing conditions. Iron speciation and mineralogy, organic matter character, as well as the likelihood for release or preservation of mineral-bound organic matter were evaluated using evidence derived from X-ray diffraction, submicrometer scale elemental mapping and X-ray absorption spectroscopy.

Materials and Methods

Field Site and Experimental Design

The DOE Rifle field site is located in northwestern Colorado on a floodplain adjacent to the Colorado River at the site of a former uranium and vanadium mill that operated between 1924 and 1958 (see Williams et al., 2011;(25) Yabusaki et al., 2007(26) for more comprehensive descriptions of the site). Currently, the site supports research activities associated with the Lawrence Berkeley National Laboratory Sustainable Systems Scientific Focus Area (SFA), whose central aim is to develop a predictive understanding of climate-induced impacts on biogeochemical functioning and carbon cycling at the watershed scale.

Mimicking the short-lived but significant increases in dissolved oxygen (DO) that accompany seasonal excursions in groundwater elevation at the Rifle site,(27) injection of oxygenated groundwater into an otherwise anoxic portion of the aquifer was designed to examine the impact of fluctuating redox conditions on biogeochemical pathways relevant to metal and carbon cycling. Aerated groundwater was injected into a formerly biostimulated well field(28) over a period of 125 days from August to December 2012; see Figure SI3.1 for a sketch of the injection setup. Prior to injection, groundwater in the well field was suboxic (DO concentration 3–7 μM; ORP from −132 to

−196 mV) with a neutral pH (7.2–7.5) and elevated ferrous iron and dissolved sulfide concentrations (53–63 μM and 0.3–3 μM, respectively). The injectate consisted of groundwater pumped from an upgradient, previously unimpacted well having low DO and Fe(II) (<20 μM and 1.5 μM, respectively) and sparged with air until the DO concentration was between 600 and 625 μM. Oxygenated groundwater was injected into six injection wells at a rate of 36 mL/min per well to achieve an aquifer DO concentration of 125–156 μM from day 0–85 (August 18 to November 11, 2012). The injectate was circulated between adjacent wells using a peristaltic pump.(25)Injection was halted from days 85–95 due to tank refilling and equipment maintenance. From day 95–125 (November 21 to December 19, 2012), the injection rate was increased 2.5-fold to achieve a target aquifer DO concentration of 313–37 μM. Following the 125-day DO injection period, circulation of groundwater between the injection wells continued through March 2013. Even in the absence of injected oxygen, this mixing system likely contributed low but steady concentrations of dissolved oxygen to the aquifer owing to the combination of gas permeable tubing and peristaltic pumps, as previously reported. (29) Groundwater conditions were allowed to evolve freely between March and April 2013 after the injection well circulation pumps were turned off, with the result being a return to the reducing conditions that existing prior to oxygen injection. Episodic groundwater measurements indicated an overall decrease in dissolved oxygen and an increase in Fe(II) by April 2013 (Table SI3.1). Groundwater temperatures averaged 14–15 °C throughout the injection well field over the course of the experiment.

Using a peristaltic pump, four precipitate samples were collected from an oxygen injection well (CG01) from a depth of ca. 4.5 m below ground surface as a part of this study: (1) in August 2012, (1 week subsequent to the first injection of oxygenated groundwater), (2) on December 19 2012 (on the last day of the second O_2 injection), (3) in March 2013 (prior to turning off cross-well mixing), and (4) 7 weeks later, at the end of April 2013. Mineral precipitates were recovered from sampling tubing prior to passage through the peristaltic pump head to minimize sample disturbance and kept fully saturated with groundwater pumped from the collection well prior to analysis. Separation of the solids was done immediately upon receiving the samples under a N_2atmosphere by vacuum filtration. Precipitates were dried and ground in the glovebox, and subsequently stored in capped serum bottles under a N_2 atmosphere. The four samples varied in color as a result of aging/reductive transformation between August 2012 and April 2013 (Supporting Information, Figure SI3.2). The initial Fe(III) precipitate was orange (Munsell color 10YR5/8); by March 2013 it became orange/brown (Dec 2012–10YR 4/6 and March 2013 10YR 4/4) and the last sample, collected in April 2013 was dark green/black (5G 1/2).

Chemical Extractions

Two chemical extractions (hydroxylamine hydrochloride and sodium pyrophosphate) were carried out on the precipitates to evaluate the composition of the mineral fraction, as well as the reactivity of the organic matter, that is, any variation in hydroxylamine- or Na pyrophosphate-extractable OM pools. The hydroxylamine hydrochloride extraction (based on Chao and Zhou, 1983(30)) estimated the amount of Fe (and impurities) bound in poorly crystalline phases in the precipitates and the amount of organic carbon released. This procedure consisted of suspending 20 mg of precipitate in 10 mL of a 0.25 M hydroxylamine hydrochloride +0.25 M HCl solution (pH 1), and reacting for 1 h in a water bath at a temperature of 50 °C under moderate shaking; the Fe-bearing phases in all samples appeared to dissolve completely as a result of this procedure.

An additional extraction was carried out by suspending 20 mg of solids in a 0.1 M sodium pyrophosphate solution (pH 10), which were reacted at room temperature for 16 h on a rotational shaker. This extraction estimates the amount of organic carbon released, as well as organic matter-bound iron. Suspensions were filtered using a 0.45 μm filter prior to ICP-MS analysis. Compositional data for all extracts were obtained using a PerkinElmer SCIEX Elan DRC II inductively coupled plasma mass spectrometer. Total organic and inorganic carbon contents in the hydroxylamine hydrochloride and pyrophosphate extracts were measured using a Shimadzu TOC-VCSH high sensitivity inorganic/organic carbon analyzer. Total organic and inorganic C were also measured for the solid phases using the carbon analyzer instrument equipped with a SSM-5000A module for solid sample analysis.

X-ray Diffraction

X-ray diffraction data were collected at the Stanford Synchrotron Radiation Lightsource (SSRL) beamline 11–3 at an energy of 12.7 keV, corresponding to a wavelength of 0.9762 Å. Scattering data were collected on a MAR 2300 detector at a sample–detector distance of ∼150 mm. Sediment powders were sandwiched in Kapton tape under a N_2 atmosphere and preserved under anaerobic conditions prior to measurements. Exposure times were of 100 s and up to five frames were collected per sample; no evidence for oxidation/phase transformation was observed between frames. Scattering data were also collected on a blank sample, which allowed for subtraction of scatter resulting from the Kapton sample mount. Calibration of the sample to detector distance was done using a lanthanum hexaboride standard (LaB_6). Data processing was carried out using the software Fit2D,(31) and background subtraction was done using the software XRD-BS.

Fe X-ray Absorption Spectroscopy

Fe K-edge extended X-ray absorption fine structure (EXAFS) spectra were collected at the Stanford Synchrotron Radiation Lightsource, at beamline 4–3, in transmission mode and fluorescence mode (Passivated Implanted Planar Silicon (PIPS) detector), using a Si111 crystal monochromator in a phi = 0 orientation. Measurements were carried out at 77 K, with a liquid nitrogen cryostat setup. The beam was fully tuned, and a Mn filter of three absorption lengths was placed in front of the PIPS detector for fluorescence measurements. Sediment powders were diluted in boron nitride powder and sealed in Teflon holders with Kapton tape. Sample preparation was carried out under nitrogen atmosphere to avoid oxidation of the Fe(II)-bearing samples, and minimal exposure to oxygen occurred while mounting the sample into the liquid nitrogen cryostat. Spectra for various Fe standard compounds (ferrihydrite, hydroxycarbonate green rust, siderite, amorphous $FeCO_3$, $Fe(OH)_2$, chukanovite, magnetite, and goethite) were collected using the same experimental setup.

X-ray energy calibration was monitored by collecting transmission data from a Fe metal foil placed between the I_1 and I_2 ionic chambers, and energy corrections were made according to the first inflection point of the reference Fe foil edge, which was set at 7111.08 eV.(32) Data extraction, processing, shell-by-shell fitting and principal component analyses and linear combination fits were carried out using the SixPack software package.(33) k^3-weighted EXAFS (k_{max} = 14 Å^{-1}) were used for shell-by-shell fits and linear combination fits (LCF). Shell-by-shell fits were carried out on Fe EXAFS for three natural ferrihydrite samples (August 2012, December 2012, and March 2013) and a synthetic ferrihydrite sample. Phase-shift and backscattering amplitude functions were generated using FEFF 7.0(34) from the crystal structures of goethite(35) for Fe–O and Fe–Fe paths. Fitting of the background-subtracted, normalized, and k^3-weighted EXAFS data were performed by filtering the dominant features of the Fourier transform to provide initial fit results for each individual shell. Values for the mean square disorder (σ^2) parameter and the amplitude reduction factor (s_o^2 = 0.90 ± 0.04) were obtained from individual shell-by-shell fits. In a final fit, all variables with the exception of σ^2 and s_{o2} were left unconstrained.

Principal component analysis (PCA) was carried out on the Fe EXAFS to constrain the minimum number of components needed to describe the data set; all four Fe EXAFS spectra were included in the PCA analysis, but no meaningful solutions could be found due to the small number of spectra and components in the data set. Linear combination fits of the most transformed sample (April 2013) were nonetheless carried out using a combination of various Fe-bearing model compounds, such as hydroxycarbonate green rust, Fe carbonate, and Fe sulfide, ferrihydrite, Fe(II) hydroxide, chukanovite, a crystalline siderite, and magnetite (Figure SI3.3). For this procedure, spectra were allowed to shift in energy during fitting, with maximum obtained shifts of 0.05 eV. Spectra for several

Fe(II)/Fe(III)–OM complexes were also included in the LCFs, but did not yield any improvement in the fit, likely because of their lack of structural order.

Scanning Transmission X-ray Microscopy

Scanning transmission X-ray microscopy (STXM) data were collected at beamline 11.0.2, at the Advanced Light Source (Lawrence Berkeley National Laboratory, CA). A Fresnel zone plate of 25 nm was used to focus a monochromatic X-ray beam onto the sample and transmission images were recorded using a scintillator-photomultiplier detector. Samples were prepared by placing a drop of each mineral suspension on a Si_3N_4 window, and allowing it to dry under a nitrogen atmosphere. The STXM chamber was continually flushed with N_2 gas prior to introducing the sample, and minimal contact with O_2 is expected to have occurred. C K-edge and Fe L-edge images were collected by scanning the sample in the x–y direction and C and Fe elemental maps were obtained by subtracting optical density images at energies below the edge from images collected above the edge of the element of interest. XANES spectra were obtained by collecting image stacks over areas of interest at energy step sizes of 0.1 eV across the main edge. Raw data were processed using the Axis2000 software(36, 37) and XANES spectra were background-corrected and normalized using the software WinXAS.(38) Peak fitting of C XANES spectra was carried out using PeakFit as shown previously. (39) Comprehensive details on the peak fitting/deconvolution procedure are given in Section 2 of the Supporting Information.

Results and Discussion

Mineralogy and Chemical Composition of the Rifle Groundwater Precipitates

The diffraction patterns shown in Figure 1a illustrate that ferrihydrite was the predominant phase present in precipitates recovered from the injection well between August 2012 and March 2013, and subsequently underwent reductive transformation by April 2013. The two broad Bragg reflections at 2θ values of ∼22 and 38 degrees are diagnostic for ferrihydrite. By April 2013, hydroxycarbonate green rust (an Fe(II)/Fe(III) hydroxycarbonate) predominates, as shown by the presence of diagnostic diffraction peaks (Figure 1a); additional poorly crystalline phases (poorly crystalline Fe(II) carbonate (siderite-like) and a poorly crystalline Fe sulfide (amorphous FeS, mackinawite-like)) are also identified, based on the presence of broad, low intensity Bragg reflections. The occurrence of a mackinawite-like iron sulfide is further supported by bulk S X-ray absorption near-edge structure (XANES) spectroscopy (Figure SI3.4). Additional crystalline phases, including quartz, calcite, and aragonite were also identified as indicated in Figure 1a.

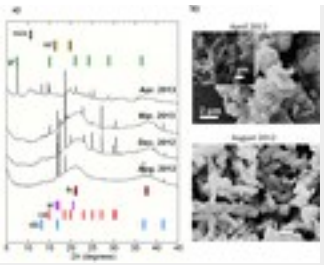

Figure 1. (a) X-ray diffraction patterns (λ = 0.9762 Å) indicate that ferrihydrite (fh) predominates between August 2012 and March 2013; hydroxycarbonate green rust (gr), a siderite-like phase or poorly crystalline Fe carbonate (sd) and a mackinawite-like phase or poorly crystalline Fe sulfide (mck) are identified in April 2013. Additional sharp reflections indicate the presence of calcite (ca), aragonite (ar) and quartz (qtz); (b) SEM images illustrate *Gallionella*-like twisted stalks in the August 2012 sample (also observed for December 2012 and March 2013 samples (not shown)). Mineral phases that exhibit a plate-like morphology are observed in April 2013; inset image for April 2013 indicates preserved stalk structures that exhibit rougher surfaces in comparison with August 2012 stalks.

SEM images illustrate that between August 2012 (Figure 1b) and March 2013 (not shown), ferrihydrite exhibits biogenic features, namely twisted stalk structures typically formed by iron(II) oxidizers of the *Gallionellaceae* family; similar types of structures have been described in detail previously, and consist of ferrihydrite particles/aggregates that precipitate within a polysaccharide-rich organic matter filament matrix(13) and may occasionally adsorb additional inorganic species or organic polymers.(40) In case of the April 2013 sample, also shown in Figure 1b, SEM imaging shows phases that exhibit a plate-like morphology typical for green rust; rounded or ill-defined phases may represent poorly crystalline iron carbonates or sulfides. Despite substantial mineralogical transformation by April 2013, the original stalk morphology is preserved, with the April 2013 inset image depicting stalks that have rougher surfaces in comparison to the original *Gallionella*-like stalks possibly due to carbonate/sulfide surface precipitation or mineral replacement.

Fe, V, and Si are the most abundant components of the four Rifle precipitates, at ∼240 mg/g Fe, 47.1 to 29.6 mg/g V and ∼11 mg/g Si (Table 1) according to hydroxylamine hydrochloride extractions. Silicate likely occurs at ferrihydrite particle surfaces as surface complexes/precipitates or Fe–Si precipitates, as suggested in previous studies on siliceous ferrihydrite.(41, 42) Elevated concentrations of vanadium occur within the Rifle aquifer,(43, 44) and V appears to be closely associated with the biogenic ferrihydrite according to micro X-ray fluorescence maps (Figure SI3.5a)). Bulk V K-edge XANES indicate that V oxidation state becomes reduced starting as early as December 2012, and becomes progressively more reduced by April 2013 (Figure SI3.5b). No further

efforts were made to understand the speciation of these inorganic impurities within the precipitates, as this was beyond the scope of our study. However, the sodium pyrophosphate extraction provides some indication that certain impurities are less intimately associated and more susceptible to changing conditions. For example, in the December 2012 sample, compared to the hydroxylamine extraction, only 10% of total iron and silicate dissolve by pyrophosphate, and half of the vanadium is released (Table 1). This suggests that half of the V in these precipitates is bound to organic matter, or possibly ferrihydrite surfaces. Additional trace elements (e.g., Cr, As, U) also show the same pattern, that is, 40–50% release by pyrophosphate as compared to hydroxylamine until December 2012, suggesting a similar binding mechanism. In contrast, for the April 2013 sample, the Na pyrophosphate solution dissolves approximately half of the hydroxylamine extractable Fe, approximately 60% Si, 88% V, 93% Cr, 120% As, and 98% U. This suggests that that Fe lability increases in this sample (Figure SI3.6a), and certain formed/remaining April 2013 Fe(II)/(III) phases are more susceptible to dissolve in a pH 10 Na pyrophosphate solution, and to release additional coprecipitated impurities. Fe(II) (hydroxy)carbonates are not likely to dissolve significantly at high pH. Generally, the Na pyrophosphate extraction procedure is used to estimate OM bound to Fe or nanoscale Fe minerals, and a significant fraction of the extracted iron may be closely associated/coprecipitated with organic matter in the April 2013 sample.

Table 1. Composition of Hydroxylamine Hydrochloride and Sodium Pyrophosphate Extracts and Total Inorganic and Organic Carbon

		Hydroxylamine hydrochloride				Sodium pyrophosphate		
		Aug. 2012	Dec. 2012	Mar. 2013	Apr. 2013	Aug. 2012	Dec. 2012	Apr. 2013
Si	mg/g	11.1	13.3	10.0	12.4	0.8	1.6	7.8
Al		0.2	0.4	1.1	0.2	0.1	0.2	0.3

	Hydroxylamine hydrochloride				Sodium pyrophosphate		
	Aug. 2012	**Dec. 2012**	**Mar. 2013**	**Apr. 2013**	**Aug. 2012**	**Dec. 2012**	**Apr. 2013**
Fe	263.0	244.0	243.7	211.2	29.0	23.3	112.7
Mn	0.9	0.8	0.5	0.6	0.2	0.5	0.3
Mg	2.9	3.5	4.7	3.0	3.1	3.0	2.4
Ca	33.4	61.9	193.7	46.1	35.4	46.7	38.7
K	0.2	0.2	0.5	0.8	0.5	0.5	1.1
V	47.1	32.7	37.7	29.6	24.1	15.2	26.1
P	6.9	na	na	na	na	na	na
S	6.6	na	na	na	na	na	na

		Hydroxylamine hydrochloride				Sodium pyrophosphate		
		Aug. 2012	**Dec. 2012**	**Mar. 2013**	**Apr. 2013**	**Aug. 2012**	**Dec. 2012**	**Apr. 2013**
Cr	ppm	48	63	28	54	25	25	50
Ni		7	12	9	7	4	4	6
Zn		13	208	646	140	13	132	157
As		6519	7674	6672	6488	2604	3908	7705
Sr		1328	1283	776	681	298	295	464
U		42	44	62	128	19	23	126
C_{org}[a]	%	1.7	1.4	3.4	2.7	0.7	0.8	4.1

carbon content of dry precipitates

	Hydroxylamine hydrochloride				Sodium pyrophosphate		
	Aug. 2012	Dec. 2012	Mar. 2013	Apr. 2013	Aug. 2012	Dec. 2012	Apr. 2013
TIC[b]	0.7	0.6	na	1			
TOC[c]	1.2	4	na	12.9			

a

Organic carbon in extract solutions.

b

Total inorganic carbon measured on dry precipitates.

c

Total organic carbon measured on dry precipitates (TC-TIC).

C measurements were also carried out on both extract solutions to determine any variation in OM pools or OM reactivity in the sample series (Table 1 and Figure SI3.6b). The organic C content measured in 0.45 µm filtered hydroxylamine hydrochloride extracts for the initial sample is 1.7%, which is comparable to the total organic content (TOC) at 1.2% obtained for the dry precipitate (Table 1). However, in later samples, hydroxylamine extractable C is significantly lower than TOC (between ~1 and 3% vs 4 and 12.9% TOC), suggesting that a majority of carbon in the March and April samples remains in particulate form; alternatively, it is also possible that the acidic pH of this solution (pH 1) caused an aggregation of the extracted OM. In case of the sodium pyrophosphate extraction, an approximately 5-fold increase in extractable OM was noted in the April 2013 sample in comparison with earlier samples. These results provide a first indication that the character of organic matter evolves during this experiment in parallel with mineralogical transformations. In particular, the

increase in pyrophosphate-extractable OM pool is notable, as it may indicate the occurrence or formation of a C pool associated with longer C turnover times.(45, 46)

Bulk and Submicrometer-Scale Iron Speciation

Based on the positions of the pre-edge and main edge, bulk Fe K-edge X-ray absorption spectroscopy near edge structure (XANES) spectra indicate that the oxidation state of iron does not change between August 2012 and March 2013 (Figure 2a). The pre-edge position for these samples is at an energy equivalent to the synthetic ferrihydrite pre-edge (7113.7 eV). In contrast, the pre-edge for the April 2013 sample shifts to lower energy (7112.4 eV), which indicates the occurrence of Fe(II), as expected in the presence of Fe(II)-bearing minerals (e.g., hydroxycarbonate green rust, Fe(II) carbonate).

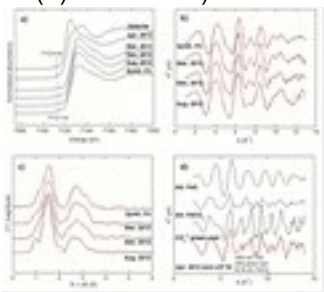

Figure 2. (a) Fe K-edge XANES spectra for the Rifle August 2012, December 2012, March 2013 and April 2013 samples, synthetic ferrihydrite and siderite (shown as reference for Fe(II)); b**)** Fe K-edge EXAFS and shell-by-shell fits for the ferrihydrite-rich Rifle samples (August 2012, December 2012 and March 2013) and synthetic ferrihydrite; see fit results in Table SI3.2; (c) Fourier transforms (FT) of EXAFS and fits for August 2012, December 2012, and March 2013 and synthetic ferrihydrite; (d) Fe K-edge EXAFS for the April 2013 sample and linear combination fit using green rust, amorphous $FeCO_3$ and amorphous FeS as model compounds; percentages indicate model compound proportions obtained from fit.

Extended X-ray absorption fine structure (EXAFS) spectra illustrate a progressive variation in EXAFS oscillations, namely an increase in intensity of the oscillation at k ~ 7.5 $Å^{-1}$ between August 2012 and March 2013 (Figure 2b). This feature has been linked to the presence of corner-sharing Fe polyhedra, and to the three-dimensional character of the ferrihydrite structure(11) and indicates a progression from a more disordered, freshly formed ferrihydrite in August 2012 to a more structurally ordered, or crystalline ferrihydrite as it ages in situ until March 2013. The EXAFS spectrum for the March 2013 sample exhibits the strongest oscillation at 7.5 $Å^{-1}$ k, and is most similar to synthetic ferrihydrite, and Fourier transforms also illustrate this similarity (Figure 2c). EXAFS shell-by-shell fits indicate a first shell Fe–O distance of 1.98 Å, with an average number of second O neighbors of ~5 for the three Rifle ferrihydrite samples (Table SI3.2). Second shell fits confirm an increase in ferrihydrite structural order, indicating an increase in the number of Fe second-neighbors along the

sample series (from ~1 to ~2) for Fe–Fe distances typical for ferrihydrite corner-sharing polyhedra (at 3.45 Å), while edge-sharing Fe polyhedra second neighbors (at ~3.03 Å) are relatively constant throughout the series (Table SI3.2).

EXAFS linear combination fitting (LCF) was carried out for the April 2013 sample to quantify the proportion of phases formed as a result of reductive transformation accompanying the decrease in aquifer redox status following cessation of cross-well mixing (Figure 2d). Several reference compounds and compound combinations were included to evaluate the best fit. In addition to green rust, amorphous $FeCO_3$, and poorly crystalline (mackinawite-like) FeS, we also included ferrihydrite, Fe(II) hydroxide ($Fe(OH)_2$), chukanovite ($Fe_2CO_3(OH)_2$), a crystalline siderite ($FeCO_3$), magnetite (Fe_3O_4), and Fe-organic compound standards, although none yielded a statistically improved fit. The best fit was obtained using hydroxycarbonate green rust, amorphous $FeCO_3$ and a mackinawite-like poorly crystalline Fe sulfide (red. chi sq. = 0.18); fit results indicate the presence of 18% poorly crystalline FeS, 30% green rust, and 52% amorphous $FeCO_3$.

At the micron scale, scanning transmission X-ray microscopy (STXM) elemental maps and Fe L-edge XANES (Figure 3a,c) indicate that ferric iron predominates in the *Gallionella*-like stalks between August 2012 and March 2013. By April 2013, both ferrous and ferric iron occur on stalks according to Fe XANES features at 708.4 and 710 eV (Figure 3c). The occurrence of Fe(III) in the April 2013 *Gallionella*-like stalks suggests the presence of residual ferrihydrite, which at this stage of the experiment underwent significant dissolution, and may thus be below the detection limits of bulk XRD and Fe EXAFS. In case of the stalk-associated Fe(II), we suggest it is bound in a Fe(II) carbonate phase that partially replaced ferrihydrite or precipitated at stalk surfaces; this assumption is based on corresponding C K-edge XANES spectra for the April 2013 stalks (Figure 3d), which show an intense peak at 290.4 eV at the carbonate resonance energy.

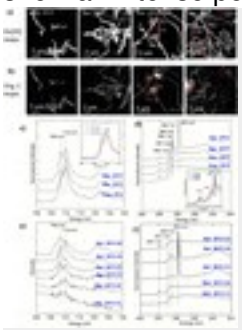

Figure 3. STXM Fe and C spectromicroscopy results (a) Fe(III) maps (710–700 eV); (b) organic C maps (288–280 eV); (c) Fe L-edge XANES for *Gallionella*-like stalks between Aug. 2012 and Apr. 2013; (d) C K-edge XANES for *Gallionella*-like stalks between Aug. 2012 and Apr. 2013; (e) Fe L-edge XANES for organic C and carbonate-rich areas indicated on Fe maps for March 2013 and April 2013 samples; March 2013 (1) and March 2013 (2): barely detectable Fe associated with organic matter aggregates; April 2013 (1): diffuse Fe(II/III)-

carbonate phase; April 2013 (2) Fe(II) carbonate; April 2013 (3) organic C-rich globule; April 2013 (4) hydroxycarbonate green rust.; (f) corresponding C K-edge XANES for organic C globules and inorganic C rich areas in March 2013 and April 2013.

Fe(II) carbonate, hydroxycarbonate green rust (Figure 3e April 2013 (2) and April 2013 (4); see Garvie et al., 1994;(47) Pantke et al. 2012(48) for typical Fe L-edges), as well as additional phases that could not be detected by bulk XRD or Fe EXAFS were also identified in the April 2013 precipitate according to STXM analyses. One such phase exhibits a thin, sheet-like morphology, and contains Fe(II), Fe(III) and carbonate according to Fe L-edge and corresponding C K-edge XANES (see spectra April 2013 (1) in Figures 3e,f). These phases are difficult to discern in the elemental maps of Figures 3a,b but additional STXM images collected at 288 eV (Figure SI3.7)depict X-ray transparent patches of approximately 1 µm in diameter. Finally, Fe L-edge combined with C K-edge mapping and spectroscopy also showed that Fe is associated with organic matter rich globules in the March and April 2013 samples. These globules, identified primarily in March 2013 (1) and (2) and April 2013 (3) exhibit variable associated Fe(II) and Fe(III) (see C K-edge and Fe L-edge XANES for Figure 3e, f). With only a few data points it is difficult to conclude as to the quantitative importance of the association of Fe(II)/(III) with these organic C rich areas. However, an apparent increase in Fe-bound OM is consistent with bulk pyrophosphate extraction results.

Carbon Distribution and Speciation on *Gallionella*-Like Stalks

C appears to be more homogeneously distributed within the *Gallionella*-like stalks between August 2012 and December 2012 in comparison with later samples (Figure 3a,b). C XANES spectra for the initial sample exhibit a spectroscopic signature (Figure 3d) that is similar to previously reported Fe oxyhydroxide-associated bacterial biomass, comprised of polysaccharides, lipopolysaccharides, hydroxylated or unsaturated lipids, and protein.(13, 40, 49, 50) Typical C XANES features include a peak at 285.1 eV (aromatic functional groups or alkene C═C bonds), a shoulder at ~287.3 eV (aliphatic groups), and a main edge peak at ~288.4 eV that results from carboxylic (288.6 eV) and amide (288.2 eV) contributions (Figure 3d). Over the duration of the aging/reductive transformation experiment, C speciation on the *Gallionella*-like stalks changed significantly, with a visible decrease in the intensity of the 285.1 and 287.3 eV features, as well as variations in the intensity and peak symmetry of the carboxyl/amide peak at ~288.4 eV. These changes are most apparent in the April 2013 stalks, together with the appearance of an intense peak at the carbonate resonance energy, ~290.4 eV (Figure 3d); as suggested above, this indicates Fe(II) carbonate surface precipitation or ferrihydrite replacement.

For each sample, peak fits for several C XANES spectra were carried out, and average peak positions and areas were used to estimate relative functional group proportions; comprehensive details about the peak-fitting procedures are given in the Supporting Information (Section 2). Initially, peak positions and intensities were fit for aromatic, aliphatic, O-alkyl and carbonate, and only one peak was used to fit the amide+carboxyl feature at ~288.4 eV; similar results were obtained whether 1s-σ* transitions were included or not in the fit. Fit results indicate that aromatic (or C=C), aliphatic, and O-alkyl functional groups decrease between August 2012 and April 2013, whereas the relative proportion of the amide+carboxyl peak increases overall (Figure 4a,b and Table SI3.3 for percentage values). The slight decrease in the amide+carboxyl relative peak area between March and April 2013 may be linked to partial OM oxidation, and related to the increase in stalk-associated carbonate (Figure 4a). However, when normalizing peak areas relative to organic C only, the increase in amide+carboxyl peak proportion stands out relative to other C types throughout the sample series (Figure 4b).

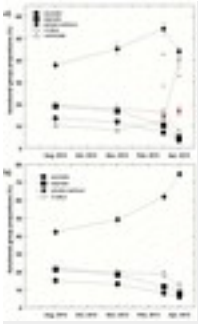

Figure 4. Functional group proportions for C XANES of stalk-associated OM between August 2012 and April 2013; peak fits were carried out using unconstrained peak positions for aromatic (~285.1 eV), aliphatic (~287.4 eV), amide+carboxyl (~288.4 eV), O-alkyl (~289.3 eV), and carbonate (~290.3 eV) functional groups. (a) variation in the proportion of all C functional groups, including carbonate; red symbols indicate examples of functional group proportions in organic C globules in the March and April 2013 samples (b) variation in the relative proportion of organic C species only as a function of time. Fit values are given in the Supporting Information, Table SI3.3.

Fit results indicate a definitive decrease of several reduced C forms (aromatic/alkene, aliphatic) and a corresponding relative increase of protein-like and carboxyl-rich carbon on stalks by the end of the experiment. By April 2013, approximately 30% of the initial organic C associated with the *Gallionella*-like stalks was lost (Figure 4a). Our fit results also indicate that ~70% of the remaining organic C on stalks consists of amide+carboxyl carbon relative to other organic C moieties (Figure 4b).
The decrease in abundance of aromatic/alkene, aliphatic, and O-alkyl functional groups suggests that organic polymers, such as lipids, lipopolysaccharides, alcohols, and possibly a fraction of

proteins underwent some degree of oxidation over the reaction period. Alternatively, desorption of an OM fraction may have caused a relative increase in functional groups such as carboxyl or the precipitation of Fe(II) carbonate phases onto the stalks. Moreover, it should also be noted that total inorganic carbonate does not increase significantly during this experiment (from ~0.6 to 1% TIC). Rather, we observe a shift in equilibrium conditions from calcium carbonates to Fe(II) carbonates. With the onset of Fe(II) reduction, groundwater conditions progress toward equilibrium with Fe(II) carbonates, which have a lower solubility.

The relative increase in amide+carboxyl on stalks suggests that these moieties, which we attribute to protein, remain associated with stalk structures despite mineralogical transformations or replacement/precipitation of secondary minerals. Proteins are known to bind strongly to mineral surfaces and resist desorption,(51-53) and this has been proposed as responsible for the formation of a stable, N-rich inner layer of organic material at mineral surfaces.(54) The abundance of carboxyl carbon on stalks by the end of the experiment can be explained by the affinity of these functional groups for iron. These changes in stalk associated OM contrast results of a recent study, which shows that the organic matter matrix of the stalk structures, composed of long-chain saturated aliphatic compounds, was preserved during diagenesis (at 250 °C–140 MPa).(55)

Character of Organic C Globules

Abundant organic C globules having diameters on the order of 2–3 μm were observed in the March and April 2013 samples (Figure 3b). C XANES data reveal a spectroscopic signature and functional group proportions occasionally comparable to the stalk-associated organic matter in the initial August 2012 sample (e.g., Figure 3f, April 2013 (3)). An enrichment in amide C is observed visually in some cases, that is, peak shifts (~0.2 eV) to lower energies (see spectra March 2013 (1) and (2) in Figure 3f). Overall, globules appear to contain a significantly greater proportion of reduced functional groups, that is, aromatic and aliphatic, as compared to the stalk materials at similar time points.

The occurrence of these organic C globules coincides with the increase in total organic C along the sample series (Table 1; Figure SI3.6b) and to the increase in Na pyrophosphate extractable OM. These globules may consist of newly added, protein-rich, (lipo)polysaccharide-rich exudates or cell components that originate from lysed microorganisms. ATR-FTIR data (Figure SI3.8) indicate an increase in bulk aliphatic, amide and carboxylic groups by April 2013 (see Table SI3.4for band assignments). Furthermore, selective measurements for dissolved organic carbon (DOC) in the supernatant solutions for the December 2012 and April 2013 precipitates also show high DOC values, at 13.8 and 32.25 mg/L, respectively. DOC is quite high in comparison with background

values of ~4 mg/L in the Rifle aquifer, and correspond to the ~3-fold increase in TOC in the precipitates during this period (Table 1).

Biomass production could have accompanied the onset of reducing conditions driving a shift in microbial community to anaerobic metal/sulfate reducers, as evidenced by the reduction of V, Fe, and SO_4^{2-}. The presence of chemolithoautotrophs (nitrifiers, S- or Fe(II)-oxidizers), or photosynthetic organisms may also be responsible for C fixation in biomass; the latter possibility is speculative based on the conditions of the aquifer groundwater (minimal light penetration in wells). The increase in particulate organic carbon could also be explained by the precipitation of dissolved organic carbon (DOC) from solution. However, given the biomass-like signature of the particulate carbon (OM globules) it is more probable that DOC served the role of electron donor for the observed metal reduction and cell growth rather than directly precipitating out of solution. Alternatively, it is also possible that a fraction of OM (e.g., lipids, polysaccharides, or (lipo)polysaccharides) desorbed from stalks, and aggregated or condensed into globules that are resistant to degradation;(56) however this pathway would not account for an increase in total organic carbon. It should also be noted that this experiment was carried out in an open system, and it is possible that there is an upstream influx of organic C; seasonal changes may also impact the organic C input.

Coupling of Fe and C Biogeochemical Cycles

By mimicking a natural rapid oxidation event followed by a return to reduced conditions, this experiment allowed us to investigate the coupled behavior of Fe and organic matter within a natural field setting. Over the course of the experiment we observed products and processes relevant to the biogeochemical cycles of Fe and C, which we suggest are linked to the oxidation/reduction experiment. However, the interpretation of our results should consider that this experiment was carried out in an open system, and thus exhibits additional complexity due to possible input from concurrent and independent upstream processes at the field site; measurements from upstream wells indicate organic C values are at their highest between 2 and 6 mg/L during the period of our experiment. We interpret our data with some precaution, but assume nonetheless that the oxygen perturbation generated a hot spot/hot moment of increased biogeochemical activity that is above background levels.

Our findings show that ferrihydrite-associated OM evolved in a manner consistent with our current understanding of organic polymer-mineral interactions. By the end of this experiment ~30% of the C associated with ferrihydrite stalks was lost, and the remaining organic C fraction was predominated by amide and/or carboxyl functional groups, of which carboxyl is known to interact strongly with mineral surfaces. It is highly likely that both desorption and partial oxidation impacted stalk OM, but according our results it is not possible to discriminate between these two phenomena. In addition to

green rust and Fe carbonate, our STXM analyses highlighted the occurrence of micron scale, mixed Fe(II)/Fe(III) carbonate phases that remain as yet unidentified; these may be transient during the bioreduction process or simply precursors to green rust formation. The observed OM complexity, heterogeneity and occurrence of Fe-OM complexes/coprecipitates also highlights the importance of using submicron scale analyses for these types of samples, as it enables a more comprehensive evaluation of Fe and C speciation at the molecular scale within specific organic structures or biominerals.

Also notable is the dramatic increase in bulk organic carbon by April 2013. This increase in biomass occurs in parallel with ferrihydrite reductive transformation, is greatly enhanced under anoxic conditions, and we suggest that it represents a significant OM pool into which carbon partitioned, or was fixed by the end of the experiment. However, it is also possible that an organic C fraction was derived from concurrent processes occurring upstream of the experiment site, or that seasonal changes are responsible for this increase. Nonetheless, the increased lability of iron by April 2013, as shown by Na pyrophosphate extractions, suggests that a significant Fe(III) fraction is associated with this OM pool, and this is surprising, since such associations are known to occur primarily under oxic, near neutral pH conditions, during the rapid precipitation of Fe(III) with organic matter. Given the hypothesized importance of Fe-OM associations in the long term preservation of organic carbon, the fact that such associations exist during the reduction phase of a redox cycling system should be considered and investigated further, as they may have a significant impact on Fe and C biogeochemical cycling.

Supporting Information

- Supporting Information includes three sections: (1) Additional descriptions of analytical methods, (2) Detailed description of C XANES peak fitting, and (3) Figures SI3.1 to 3.11, Tables SI3.1 to 3.6 (PDF)

- **PDF**
  - es5b03021_si_001.pdf (3.49 MB)

Iron and Carbon Dynamics during Aging and Reductive Transformation of Biogenic Ferrihydrite

The authors declare no competing financial interest.

Acknowledgment

This material is based upon work supported through the Lawrence Berkeley National Laboratory's Genomes-to-Watershed Scientific Focus Area. The U.S. Department of Energy (DOE), Office of Science, Office of Biological and Environmental Research funded the work under contract DE-AC02-05CH11231 (Lawrence Berkeley National Laboratory; operated by the University of California). STXM, XAS and XRD data were collected at the Advanced Light Source (ALS), Lawrence Berkeley National Laboratory and at the Stanford Synchrotron Radiation Lightsource (SSRL) at SLAC National Accelerator Laboratory. ALS and SSRL are supported by the Director, Office of Science, Office of Basic Energy Sciences of the U.S. Department of Energy.

Reference QuickView

References

This article references 56 other publications.

1. 1.

Kaiser, K.; Guggenberger, G. The role of DOM sorption to mineral surfaces in the preservation of organic matter in soils *Org. Geochem.* **2000**, 31, 711– 725 DOI: 10.1016/S0146-6380(00)00046-2

[Crossref], [CAS]

2. 2.

Mikutta, R.; Mikutta, C.; Kalbitz, K.; Scheel, T.; Kaiser, K.; Jahn, R. Biodegradation of forest floor organic matter bound to minerals via different binding mechanisms *Geochim. Cosmochim. Acta* **2007**, 71, 2569–2590 DOI: 10.1016/j.gca.2007.03.002

[Crossref], [CAS]

3. 3.

Wagai, R.; Mayer, L. M. Sorptive stabilization of organic matter in soils by hydrous iron oxides *Geochim. Cosmochim. Acta* **2007**, 71, 25– 35 DOI: 10.1016/j.gca.2006.08.047

[Crossref], [CAS]

4. 4.

Kögel-Knabner, I.; Guggenberger, G.; Kleber, M.; Kandeler, E.; Kalbitz, K.; Scheu, S.; Eusterhues, K.;Leinweber, P. Organo-mineral associations in temperate soils: Integrating biology, mineralogy, and organic matter chemistry *J. Plant Nutr. Soil Sci.* **2008**, 171, 61– 82 DOI: 10.1002/jpln.200700048

[Crossref]

5. 5.

Lalonde, K.; Mucci, A.; Ouellet, A.; Gélinas, Y. Preservation of organic matter in sediments promoted by iron*Nature* **2012**, 483, 198– 200 DOI: 10.1038/nature10855

[Crossref], [PubMed], [CAS]

6. 6.

Chenu, C.; Stotzky, G. Interactions between microorganisms and soil particles: an overview. Interactions between soil particles and microorganisms. Impact on the terrestrial ecosystem. *IUPAC Series on Analytical and Physical Chemistry of Environmental Systems*; Huang, P. M. , Eds.; John and Sons: Chichester,**2002**; p 1– 40.

7. 7.

Eusterhues, K.; Neidhardt, J.; Hädrich, A.; Küsel, K.; Totsche, K. U. Biodegradation of ferrihydrite-associated organic matter *Biogeochemistry* **2014**, 119, 0– 5 DOI: 10.1007/s10533-013-9943-0

[Crossref]

8. 8.

Jambor, J. L.; Dutrizac, J. E. Occurrence and Constitution of Natural and Synthetic Ferrihydrite, a Widespread Iron Oxyhydroxide *Chem. Rev.* **1998**, 98, 2549– 2586 DOI: 10.1021/cr970105t

[ACS Full Text], [CAS]

9. 9.

Fortin, D.; Leppard, G. G.; Tessier, A. Characteristics of lacustrine diagenetic iron oxyhydroxides *Geochim. Cosmochim. Acta* **1993**, 57, 4391– 4404 DOI: 10.1016/0016-7037(93)90490-N

[Crossref], [CAS]

10. 10.

Kennedy, C.; Scott, S.; Ferris, F. Hydrothermal phase stabilization of 2-line ferrihydrite by bacteria *Chem. Geol.* **2004**, 212, 269– 277 DOI: 10.1016/j.chemgeo.2004.08.017

[Crossref], [CAS]

11. 11.

Toner, B. M.; Santelli, C. M.; Marcus, M. A.; Wirth, R.; Chan, C. S.; McCollom, T.; Bach, W.; Edwards, K. J.Biogenic iron oxyhydroxide formation at mid-ocean ridge hydrothermal vents: Juan de Fuca Ridge *Geochim. Cosmochim. Acta* **2009**, 73, 388– 403 DOI: 10.1016/j.gca.2008.09.035

[Crossref], [CAS]

12. 12.

Chan, C. S.; De Stasio, G.; Welch, S. A.; Girasole, M.; Frazer, B. H.; Nesterova, M. V.; Fakra, S.;Banfield, J. F. Microbial polysaccharides template assembly of nanocrystal fibers *Science* **2004**, 303, 1656–1658 DOI: 10.1126/science.1092098

[Crossref], [PubMed], [CAS]

13. 13.

Chan, C. S.; Fakra, S. C.; Edwards, D. C.; Emerson, D.; Banfield, J. F. Iron oxyhydroxide mineralization on microbial extracellular polysaccharides *Geochim. Cosmochim. Acta* **2009**, 73, 3807– 3818 DOI: 10.1016/j.gca.2009.02.036

[Crossref], [CAS]

14. 14.

Melton, E. D.; Swanner, E. D.; Behrens, S.; Schmidt, C.; Kappler, A. The interplay of microbially mediated and abiotic reactions in the biogeochemical Fe cycle *Nat. Rev. Microbiol.* **2014**, 12, 797– 808 DOI: 10.1038/nrmicro3347

[Crossref], [PubMed], [CAS]

15. 15.

Posth, N.; Canfield, D. E.; Kappler, A. Biogenic Fe(III) minerals: from formation to diagenesis and preservation in the rock record *Earth-Sci. Rev.* **2014**, 135, 103– 121 DOI: 10.1016/j.earscirev.2014.03.012

[Crossref], [CAS]

16. 16.

Fabisch, M.; Freyer, G.; Johnson, C. A.; Büchel, G.; Akob, D. M.; Neu, T. R.; Küsel, K. Dominance of '*Gallionella capsiferriformans*' and heavy metal association with *Gallionella*-like stalks in metal-rich pH 6 mine water discharge *Geobiology* **2015**, 1– 23 DOI: 10.1111/gbi.12162

[Crossref], [PubMed]

17. 17.

Borch, T.; Kretzschmar, R.; Kappler, A.; van Cappellen, P.; Ginder-Vogel, M.; Voegelin, A.; Campbell, K.Biogeochemical Redox Processes and their impact on contaminant dynamics *Environ. Sci. Technol.* **2010**,44, 15– 23 DOI: 10.1021/es9026248

[ACS Full Text], [CAS]

18. 18.

Kukkadapu, R. K.; Zachara, J. M.; Fredrickson, J. K.; Kennedy, D. W. Biotransformation of two-line silica-ferrihydrite by a dissimilatory Fe(III)-reducing bacterium: formation of carbonate green rust in the presence of phosphate *Geochim. Cosmochim. Acta* **2004**, 68, 2799– 2814 DOI: 10.1016/j.gca.2003.12.024

[Crossref], [CAS]

19. 19.

Borch, T.; Masue, Y.; Kukkadapu, R. K.; Fendorf, S. Phosphate imposed limitations on biological reduction and alteration of ferrihydrite *Environ. Sci. Technol.* **2007**, 41, 166– 72 DOI: 10.1021/es060695p

[ACS Full Text], [CAS]

20. 20.

Hansel, C. M.; Learman, D. R.; Lentini, C. J.; Ekstrom, E. B. Effect of adsorbed and substituted Al on Fe(II)-induced mineralization pathways of ferrihydrite *Geochim. Cosmochim. Acta* **2011**, 75, 4653– 4666 DOI: 10.1016/j.gca.2011.05.033

[Crossref], [CAS]

21. 21.

Piepenbrock, A.; Dippon, U.; Porsch, K.; Appel, E.; Kappler, A. Dependence of microbial magnetite formation on humic substance and ferrihydrite concentrations *Geochim. Cosmochim. Acta* **2011**, 75, 6844–6858 DOI: 10.1016/j.gca.2011.09.007

[Crossref], [CAS]

22. 22.

Fritzsche, A.; Bosch, J.; Rennert, T.; Heister, K.; Braunschweig, J.; Meckenstock, R. U.; Totsche, K. U. Fast microbial reduction of ferrihydrite colloids from a soil effluent *Geochim. Cosmochim. Acta* **2012**, 77, 444–456 DOI: 10.1016/j.gca.2011.10.037

[Crossref], [CAS]

23. 23.

Shimizu, M.; Zhou, J.; Schröder, C.; Obst, M.; Kappler, A.; Borch, T. Dissimilatory reduction and transformation of ferrihydrite-humic acid coprecipitates *Environ. Sci. Technol.* **2013**, 47, 13375– 13384 DOI: 10.1021/es402812j

[ACS Full Text], [CAS]

24. 24.

Kappler, A.; Benz, M.; Schink, B.; Brune, A. Electron shuttling via humic acids in microbial iron(III) reduction in a freshwater sediment *FEMS Microbiol. Ecol.* **2004**, 47 (1) 85– 92 DOI: 10.1016/S0168-6496(03)00245-9

[Crossref], [PubMed], [CAS]

25. 25.

Williams, K. H.; Long, P. E.; Davis, J. A.; Wilkins, M. J.; N'Guessan, A. L.; Steefel, C. I.; Yang, L.;Newcomer, D.; Spane, F. A.; Kerkhof, L. J.; McGuinness, L.; Dayvault, R.; Lovley, D. R. Acetate Availability and its Influence on Sustainable Bioremediation of Uranium-Contaminated Groundwater *Geomicrobiol. J.***2011**, 28, 519– 539 DOI: 10.1080/01490451.2010.520074

[Crossref], [CAS]

26. 26.

Yabusaki, S. B.; Fang, Y.; Long, P. E.; Resch, C. T.; Peacock, A. D.; Komlos, J.; Jaffe, P. R.; Morrison, S. J.;Dayvault, R. D.; White, D. C.; Anderson, R. T. Uranium removal from groundwater via in situ biostimulation: field-scale modeling of transport and biological processes *J. Contam. Hydrol.* **2007**, 93, 216– 235 DOI: 10.1016/j.jconhyd.2007.02.005

[Crossref], [PubMed], [CAS]

27. 27.

Yabusaki, S. B.; Fang, Y.; Williams, K. H.; Murray, C. J.; Ward, A. L.; Dayvault, R. D.; Waichler, S. R.;Newcomer, D. R.; Spane, F. A.; Long, P. E. Variably saturated flow and multicomponent biogeochemical reactive transport modeling of a uranium bioremediation field experiment *J. Contam. Hydrol.* **2011**, 126,271– 290 DOI: 10.1016/j.jconhyd.2011.09.002

[Crossref], [PubMed], [CAS]

28. 28.

Luef, B.; Frischkorn, K. R.; Wrighton, K. C.; Holman, H-Y.N.; Birada, G.; Thomas, B. C.; Singh, A.;Williams, K. H.; Siegerist, C. E.; Tringe, S. G.; Downing, K. H.; Comolli, L. R.; Banfield, J. F. Diverse uncultivated ultra-small bacterial cells in groundwater *Nat. Commun.* **2015**, 6, 6372 DOI: 10.1038/ncomms7372

[Crossref], [PubMed], [CAS]

29. 29.

Williams, K. H.; Wilkins, M. J.; N'Guessan, A. L.; Arey, B.; Dodova, E.; Dohnalkova, A.; Holmes, D.;Lovley, D. R.; Long, P. E. Field evidence of selenium bioreduction in a uranium contaminated aquifer *Environ. Microbiol. Rep.* **2013**, 5, 444– 452 DOI: 10.1111/1758-2229.12032

[Crossref], [PubMed], [CAS]

30. 30.

Chao, T. T.; Zhou, L. Extraction techniques for selective dissolution of amorphous iron-oxides from soils and sediments *Soil Sci. Soc. Am. J.* **1983**, 47, 225– 232 DOI: 10.2136/sssaj1983.03615995004700020010x

[Crossref], [CAS]

31. 31.

Hammersley, A. P.; Svensson, S. O.; Hanfland, M.; Fitch, A. N.; Häusermann, D. Two-dimensional detector software: from real detector to idealised image or two-theta scan *High Pressure Res.* **1996**, 14, 235– 248DOI: 10.1080/08957959608201408

[Crossref]

32. 32.

Wilke, M.; Farges, F.; Petit, P.-E.; Brown, G. E., Jr.; Martin, F. Oxidation state and coordination of Fe in minerals: an Fe K-XANES spectroscopic study *Am. Mineral.* **2001**, 86, 714– 730 DOI: 10.2138/am-2001-5-612

[Crossref], [CAS]

33. 33.

Webb, S. M. SIXPack: a graphical user interface for XAS analysis using IFEFFIT *Phys. Scr.* **2005**, T115,1011– 1014 DOI: 10.1238/Physica.Topical.115a01011

[Crossref], [CAS]

34. 34.

Ankudinov, A. L.; Rehr, J. J. Relativistic calculations of spin-dependent X-ray-absorption spectra *Phys. Rev. B: Condens. Matter Mater. Phys.* **1997**, 56, R1712– R1716 DOI: 10.1103/PhysRevB.56.R1712

[Crossref], [CAS]

35. 35.

Hoppe, W. Über die kristallstruktur von α-AlOOH (diaspor) und α-FeOOH nadeleisenerz *Z. Kristallogr. - Cryst. Mater.* **1940**, 103, 73– 89 DOI: 10.1524/zkri.1941.103.1.73

[Crossref], [CAS]

36. 36.

Hitchcock, A. P. AXis2000 software (ver2.1n), **2000**. http://unicorn.cmaster.ca/aXis2000.html.

37. 37.

Hitchcock, A. P. Chemical mapping with soft X-ray spectromicroscopy *Am. Lab.* **2001**, 33, 30– 36

[CAS]

38. 38.

Ressler, T. *WinXAS version 3.x Manual*; TU Berlin, **2009**.

39. 39.

Keiluweit, M.; Bougoure, J. J.; Zeglin, L. H.; Myrold, D. D.; Weber, P. K.; Pett-Ridge, J.; Kleber, M.;Nico, P. S. Nano-scale investigation of the association of microbial nitrogen residues with iron (hydr)oxides in a forest soil O-horizon *Geochim. Cosmochim. Acta* **2012**, 95, 213– 226 DOI: 10.1016/j.gca.2012.07.001

[Crossref], [CAS]

40. 40.

Bennett, S. A.; Toner, B. M.; Barco, R.; Edwards, K. J. Carbon adsorption onto Fe oxyhydroxide stalks produced by a lithotrophic iron-oxidizing bacteria *Geobiology* **2014**, 12, 146– 156 DOI: 10.1111/gbi.12074

[Crossref], [PubMed], [CAS]

41. 41.

Dyer, L. G.; Chapman, K. W.; English, P.; Saunders, M.; Richmond, W. R. Insights into the crystal and aggregatee structure of Fe^{3+} oxide/silica co-precipitates *Am. Mineral.* **2012**, 97, 63– 69 DOI: 10.2138/am.2011.3874

[Crossref], [CAS]

42. 42.

Cismasu, A. C.; Michel, F. M.; Tcaciuc, A. P.; Brown, G. E., Jr. Properties of impurity-bearing ferrihydrite III. Effects of Si on the structure of 2-line ferrihydrite *Geochim. Cosmochim. Acta* **2014**, 133, 168– 185 DOI: 10.1016/j.gca.2014.02.018

[Crossref], [CAS]

43. 43.

Ortiz-Bernad, I.; Anderson, R. T.; Vrionis, H. A.; Lovley, D. R. Vanadium Respiration by Geobacter metallireducens: Novel Strategy for In Situ Removal of Vanadium from Groundwater *Appl. Environ. Microb.***2004**, 70, 3091– 3095 DOI: 10.1128/AEM.70.5.3091-3095.2004

[Crossref], [PubMed], [CAS]

44. 44.

Yelton, A. P.; Williams, K. H.; Fournelle, J.; Wrighton, K. C.; Handley, K. M.; Banfield, J. F. Vanadate and acetate biostimulation of contaminated sediments decreases diversity, selects for specific taxa, and decreases aqueous V^{5+} concentration *Environ. Sci. Technol.* **2013**, 47, 6500– 6509 DOI: 10.1021/es4006674

[ACS Full Text], [CAS]

45. 45.

Kaiser, M.; Ellerbrock, R. H. Functional characterization of soil organic matter fractions different in solubility originating from a long-term field experiment *Geoderma* **2005**, 127, 196– 206 DOI: 10.1016/j.geoderma.2004.12.002

[Crossref], [CAS]

46. 46.

Habermann, J.; Ellerbrock, R. H.; Remus, R.; Augustin, J.; Matschullat, J. Sequential extraction of a carbon-14 labeled soil from Halle, Germany *Geophys. Res. Abtracts* **2006**, 8, 06072

47. 47.

Garvie, L. A. J.; Craven, A. J.; Brydson, R. Use of electron-energy loss near-edge fine structure in the study of minerals *Am. Mineral.* **1994**, 79, 411– 425

[CAS]

48. 48.

Pantke, C.; Obst, M.; Benzerara, K.; Morin, G.; Ona-Nguema, G.; Dippon, U.; Kappler, A. Gree n rust formation during Fe(II) oxidation by the nitrate-reducing *Acidovorax sp.* strain BoFeN1 *Environ. Sci. Technol.***2012**, 46, 1439– 1446 DOI: 10.1021/es2016457

[ACS Full Text], [CAS]

49. 49.

Miot, J.; Benzerara, K.; Obst, M.; Kappler, A.; Hegler, F.; Schädler, S.; Bouchez, C.; Guyot, F.; Morin, G.Extracellular iron biomineralization by photoautotrophic iron-oxidizing bacteria *Appl. Environ. Microb.* **2009**,75, 5586– 5591 DOI: 10.1128/AEM.00490-09

[Crossref], [PubMed], [CAS]

50. 50.

Chan, C. S.; Fakra, S. C.; Emerson, D.; Fleming, E. J.; Edwards, K. J. Lithotrophic iron-oxidizing bacteria produce organic stalks to control mineral growth: implications for biosignature formation *ISME J.* **2011**, 5,717– 727 DOI: 10.1038/ismej.2010.173

[Crossref], [PubMed], [CAS]

51. 51.

Hlady, V.; Buijs, J. Protein adsorption on solid surfaces *Curr. Opin. Biotechnol.* **1996**, 7, 72– 77 DOI: 10.1016/S0958-1669(96)80098-X

[Crossref], [PubMed], [CAS]

52. 52.

Chevallier, T.; Muchaonyerwa, P.; Chenu, C. Microbial utilisation of two proteins adsorbed to a vertisol clay fraction: toxin from Bacillus thuringiensis subsp. tene brionis and bovine serum albumin *Soil Biol. Biochem.***2003**, 35, 1211– 1218 DOI: 10.1016/S0038-0717(03)00182-2

[Crossref], [CAS]

53. 53.

Omoike, A.; Chorover, J. Adsorption to goethite of extracellular polymeric substances from *Bacillus subtilisGeochim. Cosmochim. Acta* **2006**, 70, 827– 838 DOI: 10.1016/j.gca.2005.10.012

[Crossref], [CAS]

54. 54.

Kleber, M.; Sollins, P.; Sutton, R. A conceptual model of organo-mineral interactions in soils: self-assembly of organic molecular fragments into zonal structures on mineral surfaces *Biogeochemistry* **2007**, 85, 9– 24DOI: 10.1007/s10533-007-9103-5

[Crossref]

55. 55.

Picard, A.; Kappler, A.; Schmid, G.; Quaroni, L.; Obst, M. Experimental diagenesis of organo-mineral structures formed by microaerophilic Fe(II)-oxidizing bacteria *Nat. Commun.* **2015**, 6, 6277 DOI: 10.1038/ncomms7277

[Crossref], [PubMed], [CAS]

56. 56.

Lutzow, M. V.; Kogel-
Knabner, I.; Ekschmitt, K.; Matzner, E.; Guggenberger, G.; Marschner, B.; Flessa, H.Stabilizati on of organic matter in temperate soils: mechanisms and their relevance under different soil

conditions - a review *Eur. J. Soil Sci.* **2006**, 57, 426– 445 DOI: 10.1111/j.1365-2389.2006.00809.x

[Crossref], [CAS]